ACS Sustainable Resource Management

pubs.acs.org/acssrm

Article

Sustainable Valorization of Banana Peel Waste into a Biochar-Integrated BiOBr/rGO Ternary Nanocomposite for Photocatalytic Decomposition of Prednisolone

Mano Ranjan Barik, Ankita Ram, and Sushanta Kumar Badamali*

Cite This: https://doi.org/10.1021/acssusresmgt.5c00430

Read Online

ACCESS | Metrics & More | Article Recommendations | Supporting Information

ABSTRACT: The persistent occurrence of steroidal pharmaceuticals such as prednisolone (PS) in aquatic systems poses significant ecological threats due to their endocrine-disrupting potential and resistance to conventional treatment technologies. In this study, banana peel waste was valorized into biochar and integrated with BiOBr and rGO to synthesize a ternary BiOBr/rGO/biochar (BiGB5) nanocomposite via a facile coprecipitation route. X-ray diffraction revealed distinct reflections corresponding to individual phases, confirming the coexistence of separate crystalline structures. FTIR spectra exhibited strong absorption around 600 cm^{-1}, attributed to Bi−O vibrations, while FESEM and HRTEM analyses demonstrated well-defined morphologies. XPS confirmed the presence of Bi^{3+}, Br^{-}, C, and O species. The composite exhibited a specific surface area of 8.9 m^2 g^{-1}. PL studies indicated suppressed electron−hole recombination, and UV−vis diffuse reflectance spectroscopy determined an optical band gap of 2.79 eV. Under sunlight irradiation, BiGB5 achieved ∼91% degradation of PS within 180 min, surpassing pristine BiOBr and binary counterparts. The superior photocatalytic efficiency was attributed to synergistic charge transfer via rGO and abundant active sites on biochar, facilitating hydroxyl radical (•OH) generation. LC-MS analysis enabled a proposed degradation pathway, establishing BiGB5 as a sustainable photocatalyst for efficient removal of recalcitrant pharmaceutical contaminants.

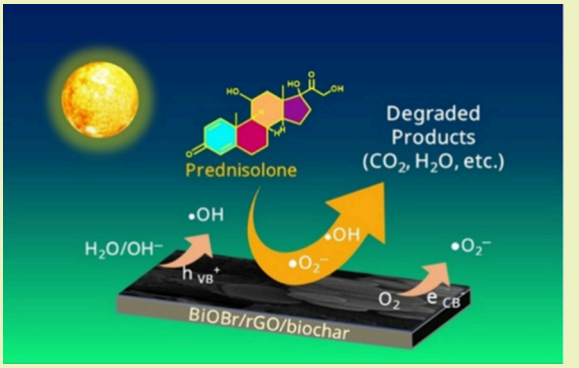

KEYWORDS: *photocatalysis, biochar, nanocomposite, wastewater, pharmaceutical, prednisolone*

1. INTRODUCTION

The worldwide surge in population growth has experienced a proportional increase in demand for food, energy, healthcare, household materials, etc. Apart from basic needs, the food and pharmaceutical industries play a vital role in affording a life free from hunger and disease. Pharmaceuticals such as steroid medicines, including corticosteroids and anabolic steroids, are widely used for treating inflammatory, autoimmune, and hormonal diseases. As of 2024, the global steroid market is valued at approximately USD 3451.2 million,[1,2] among which prednisolone (PS) is a synthetic glucocorticoid widely used for its anti-inflammatory and immunosuppressive properties in treating conditions such as asthma, rheumatoid arthritis, and autoimmune disorders.[3,4] However, its overuse poses serious health risks and environmental hazards as PS lacks natural degradation into harmless components. These residual PS enter water bodies through human and animal excretion and pharmaceutical waste, leading to contamination of water streams.[5,6] The PS residues alter microbial diversity, affecting soil fertility and plant growth. The continuous exposure of PS in water and soil leads to accumulation in organisms, affecting entire food chains.[7,8] Therefore, it is crucial to eliminate the residues associated with PS to minimize the environmental risks.

Several remediation techniques have been employed for the removal of PS, including traditional methods such as coagulation, adsorption, membrane separation, and biodegradation.[9] These remediations are often expensive, are inconsistent, and lead to the generation of secondary waste materials. On the other hand, advanced oxidation processes (AOPs) such as UV/H_2O_2, O_3/H_2O_2, Fenton, photo-Fenton, and photocatalysis commonly utilize atomic oxygen or oxidizing radicals for the degradation of organic pollutants. Among them, photocatalytic degradation is considered to be the most effective remediation technique for PS degradation. Furthermore, photocatalysis operates under mild conditions,

Received: August 27, 2025
Revised: December 15, 2025
Accepted: December 16, 2025

utilizes renewable solar energy, and requires minimal chemical additives.[10,11]

Semiconductor-based photocatalysts such as TiO_2, ZnO, BiOBr, WO_3, rGO, g-C_3N_4, and CdS typically function on the mechanism of light adsorption followed by the generation of electron-hole pairs (e^-−h^+).[12,13] These (e^-−h^+) pairs react with the water and oxygen present in the reaction to produce hydroxyl (•OH) and superoxide ($\bullet O_2^-$) radicals, which degrade the pollutants to either smaller fragments or mineralize into CO_2 and H_2O. Nevertheless, the major challenge encountered by the charge carriers is the fast recombination due to the electrostatic force of attraction that exists between the (e^-−h^+) pairs. Rapid recombination causes energy loss, thereby limiting the overall performance of the photocatalytic system.[14] To overcome these recombination issues, recently nanocomposite-based photocatalysts were developed, which combine two or more materials that can potentially enhance charge separation and prolong the lifetime of photogenerated (e^-−h^+) pairs.

BiOBr is an efficient photocatalyst due to its visible-light-responsive band gap of ∼2.8 eV, offering high stability, low cost, and eco-friendliness, making it suitable for large-scale environmental remediation.[15] Similarly, reduced graphene oxide (rGO) with its 2D graphene-like nanosheet structure provides high surface area, excellent charge transfer, and strong adsorption/photocatalytic activity.[16] Biochar, produced from biomass pyrolysis, enhances performance through its porous structure, large surface area, and electron transfer ability, apart from promoting a sustainable "waste-to-wealth" concept.[17] Although these individual photocatalysts possess certain unique advantages, their individual performance is often marred by certain drawbacks. Therefore, BiOBr/rGO/biochar nanocomposites are essential to enhance electron-hole separation, suppress recombination, and increase active sites, thereby significantly boosting photocatalytic efficiency.

Studies on PS degradation available in the open literature revealed that UV radiation,[18] UV/chlorine oxidation,[19] and the electro-Fenton process[20] resulted in 18, 40, and 74% efficiency, respectively, within 1−2 h of reaction. This study focuses on developing a cost-effective and highly efficient ternary BiOBr/rGO/biochar composite using a precipitation method. The uniqueness of this work lies in the synergistic integration of BiOBr, a visible-light-responsive photocatalyst; rGO, a conductive material that facilitates rapid electron transport; and biochar, a sustainable, porous carbon material derived from waste, which enhances adsorption and supports charge separation. This composite not only addresses preventing the recombination issue prevalent in single photocatalysts but also contributes to a "waste-to-wealth" approach through the use of biochar. Unlike traditional methods that often rely on artificial UV sources or harsh conditions, this research utilizes widely available sunlight and water as a solvent, thereby demonstrating an environmentally friendly, low-cost, and effective photocatalytic system. The reaction parameters, such as catalyst dosages, initial PS concentration, time duration, and kinetics study, were extensively studied. Additionally, this proposal aims to evaluate the durability and recyclability of the catalyst, along with the scavenger's study and LC MS analysis for the elucidation of a plausible degradation pathway toward PS mineralization.

2. EXPERIMENTAL SECTION

2.1. Preparation of the BiGB5 Nanocomposite. Graphene oxide (GO) and reduced graphene oxide (rGO) were synthesized using a modified version of Hummers' method, following Mei et al.[21] with minor modifications. Biochar from banana peels was prepared following the procedure that was reported by Nadew et al.[22] The composite preparation was carried out by adding 0.595 g of KBr in 100 mL of deionized water as the bromine source (Scheme 1). Then,

Scheme 1. Schematic Representation of the Synthesis of the BiGB5 Composite

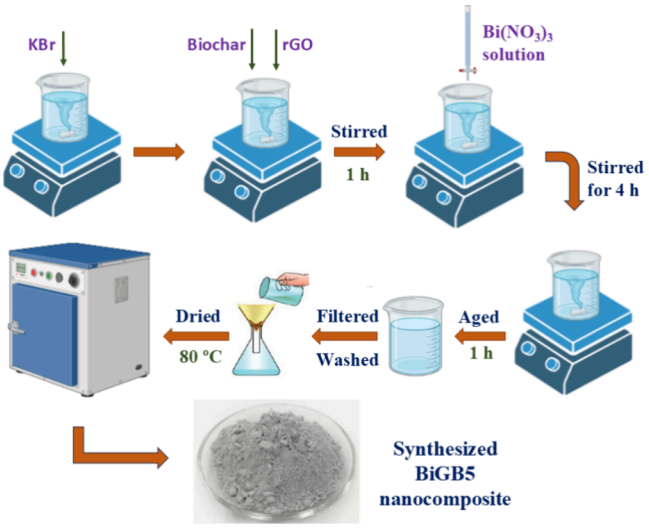

75 mg of rGO (for a 5% w/w ratio) and the same amount of biochar were added to the KBr solution and stirred vigorously for 1 h. Then, 2.4 g of $Bi(NO_3)_3{\cdot}5H_2O$ was taken with 9 mL of acetic acid in a 100 mL aqueous solution and stirred for an hour. The $Bi(NO_3)_3$ solution was gradually introduced into the KBr solution with continuous magnetic stirring, and the mixture was stirred for 4 h at ambient temperature, followed by aging the resultant suspension for another 1 h. The precipitates were obtained through filtration, washed thoroughly four times using distilled water and ethanol, and subsequently dried at 80 °C overnight to produce the final composite material with 90 wt % of BiOBr, 5 wt % of r-GO, and 5 wt % of biochar (BiGB5). In a similar process, BiG5 (95% BiOBr and 5% rGO, without biochar) and BiOBr (without using rGO and biochar) were prepared.

3. RESULTS AND DISCUSSION

3.1. Catalyst Characterization. *3.1.1. XRD Analysis.* The crystalline structure and phase composition of the materials were investigated using X-ray diffraction (XRD) study, and the corresponding diffraction patterns are presented in Figure 1a. The patterns were recorded for individual components such as BiOBr, biochar, rGO, and the synthesized composite BiGB5. The XRD pattern of pure BiOBr exhibits distinct and sharp diffraction peaks at 2θ values 10.9, 25.1, 31.5, 32.3, 39.2, 46.3, 50.5, 53.4, and 57.1° corresponding to the (001), (101), (102), (110), (112), (200), (104), (211), and (212) planes. These reflections are perfectly matched with the standard tetragonal phase of BiOBr (JCPDS No. 73-2061), confirming the high crystallinity and phase purity of the synthesized BiOBr.[23,24] The biochar sample displays a broad peak in the range of 20−30°, which is indicative of its amorphous carbonaceous nature. Weak diffraction features observed may correspond to residual mineral content or partially graphitized structures.[25] The XRD pattern of rGO shows two broad peaks centred around 2θ

https://doi.org/10.1021/acssusresmgt.5c00430
ACS Sustainable Resour. Manage. XXXX, XXX, XXX−XXX

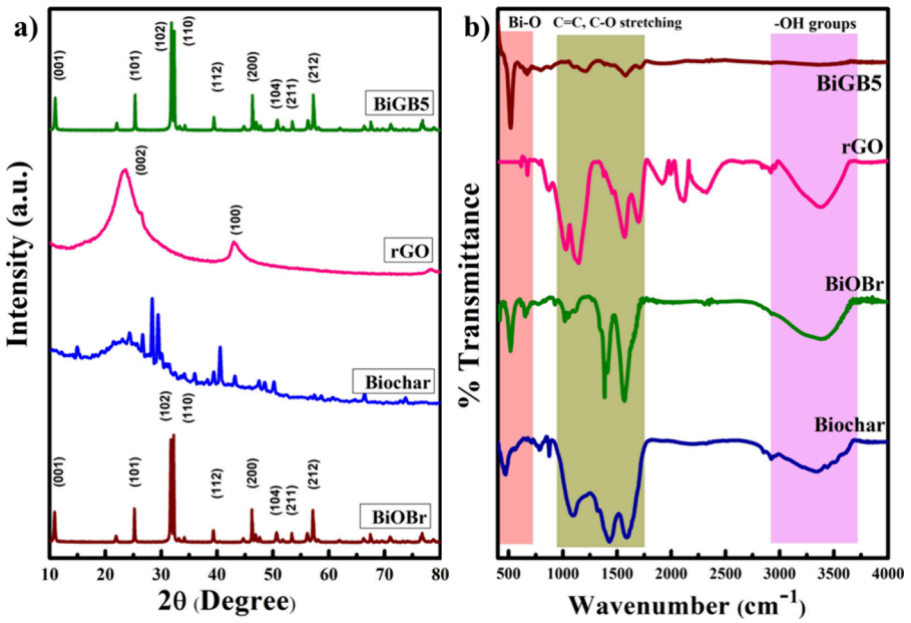

Figure 1. XRD (a) and FT IR (b) analyses of photocatalysts.

values of 24 and 43°, which are due to the (002) and (100) planes of rGO, respectively.[26] In the case of the BiGB5 material, the diffraction peaks corresponding to BiOBr are retained, signifying that the BiOBr phase is preserved within the composite.

The crystallite sizes of BiOBr and BiGB5 were determined using Debye−Scherrer's equation:

$$D = \frac{k\lambda}{\beta\cos\theta} \quad (1)$$

where D is the crystallite size, k is the shape factor (0.9), λ is the X-ray wavelength (1.54 Å), β is the full width at half maximum (FWHM), and θ is the Bragg's angle. The calculated average crystallite sizes for tetragonal BiOBr and BiGB5 were 34.9 and 37.5 nm, respectively.

3.1.2. FT IR Analysis. The Fourier transform infrared spectroscopy (FTIR spectra) of BiOBr, biochar, rGO, and the synthesized composite are depicted in Figure 1b, which explains the functional groups and chemical interactions in the catalyst. In the case of BiOBr, a strong absorption band was observed in the region below 600 cm^{-1}, corresponding to the stretching vibrations of Bi−O bonds, confirming the presence of the BiOBr matrix. The spectrum of biochar shows multiple characteristic peaks, particularly in the region 1000−1700 cm^{-1}, which can be attributed to C═C aromatic stretching and C−O stretching, indicating the presence of various oxygenated functionalities on the carbon surface.[27] Furthermore, broad absorptions between 3000 and 3600 cm^{-1} are associated with O−H stretching vibrations, suggesting the surface hydroxyl groups.[28] Similarly, the rGO spectrum displays noticeable features in the 1000−1700 cm^{-1} region due to C═C and C−O stretching, which are characteristic of sp^2-hybridized carbon structures and oxygen-containing functional groups. Peaks in the region 1800−2300 cm^{-1} correspond to the C≡C and adsorbed CO_2 in the rGO matrix.[29] The broad band near 3400 cm^{-1} is due to the hydroxyl groups. In the case of the composite BiGB5 material, the FTIR spectrum reveals the retention of all key functional group signals from BiOBr, rGO, and biochar. Notably, the appearance of Bi−O and −OH groups in the composite spectrum confirms the successful integration of the individual components. The interaction between BiOBr and the carbon-based materials is indicated by the slight shifts or intensity changes, suggesting chemical or strong interfacial interaction.

3.1.3. FE SEM Analysis. Field emission scanning electron microscopy (FE SEM) was employed to investigate the morphological characteristics of pristine BiOBr, rGO, biochar, and the BiGB5 composite. The representative images are presented in Figure 2. BiOBr, as shown in Figure 2a, displays a

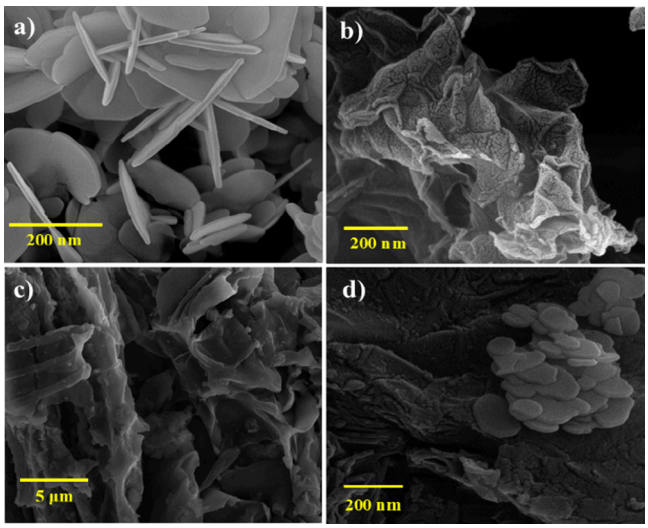

Figure 2. FE SEM images and mapping of BiOBr (a), rGO (b), biochar (c), and BiGB5 (d).

characteristic disc-shaped morphology composed of uniformly stacked lamellar nanosheets. This hierarchical structure provides an extended surface area and numerous exposed reactive facets, which are advantageous for enhancing light absorption and catalytic activity in photocatalytic applications. Figure 2b depicts the ultrathin, wrinkled sheet of rGO. This morphology is indicative of the successful reduction of

https://doi.org/10.1021/acssusresmgt.5c00430
ACS Sustainable Resour. Manage. XXXX, XXX, XXX−XXX

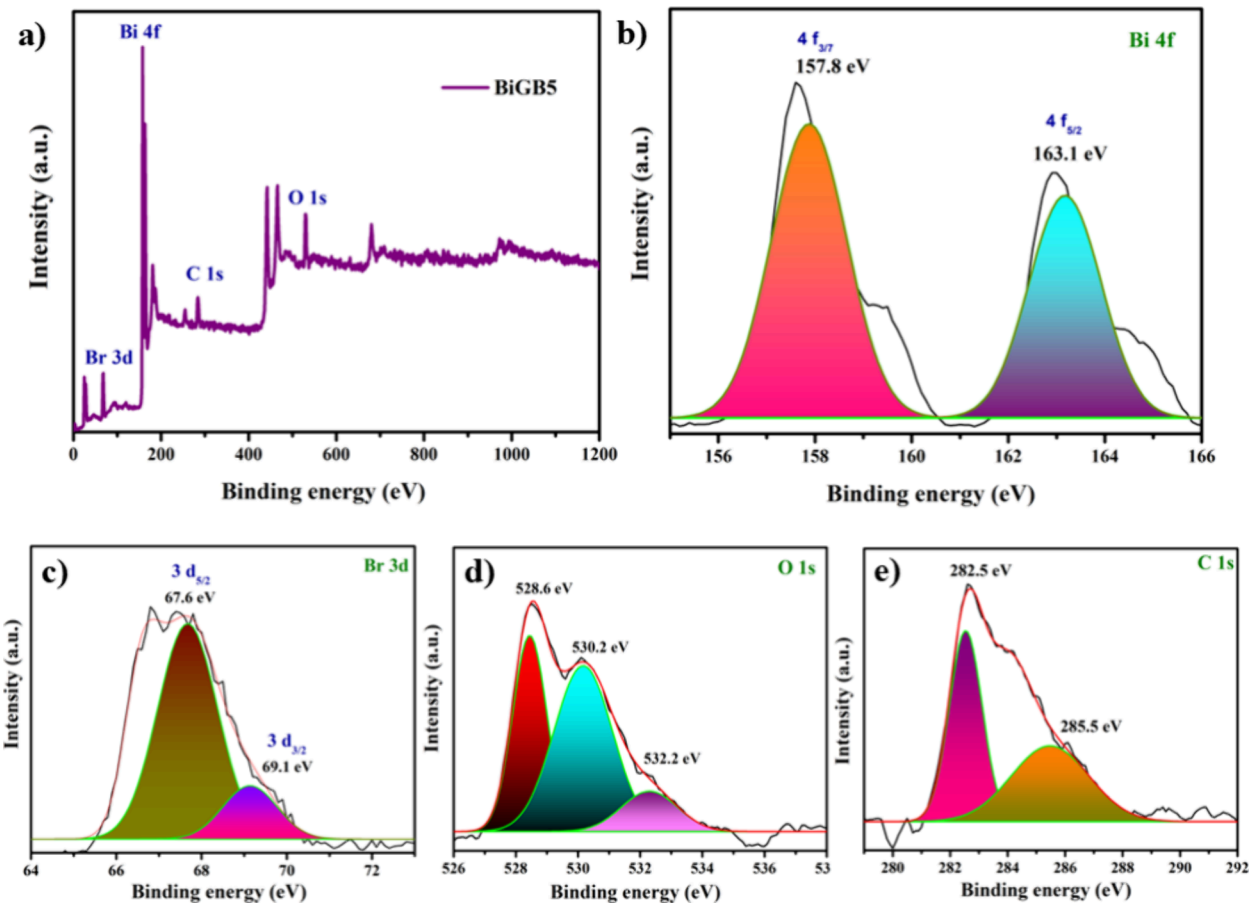

Figure 3. XPS survey of BiGB5 (a), high-resolution binding spectra of Bi 4f (b), Br 3d (c), O 1s (d), and C 1s (e).

graphene oxide, resulting in highly conductive and flexible layers. The high surface area and π-conjugated system of rGO promote rapid electron transfer and provide active sites for interfacial interactions within the composite matrix. Biochar, as shown in Figure 2c, exhibits a porous and irregular surface structure with sponge-like features. The porous nature, which arises from the thermal decomposition of biomass, supports the improved adsorption capacity and diffusion of products. In the BiGB5 composite (Figure 2d), the nanostructure reveals a well-integrated network of BiOBr nanosheets anchored onto rGO surfaces, with biochar particles uniformly embedded within the framework. The EDAX pattern (Figure S1) also reveals distinct peaks corresponding to the elemental presence of Bi, O, C, and Br, confirming the successful fabrication of BiOBr, rGO, and biochar in the material. This hybrid architecture facilitates better interfacial contact between the components, enabling efficient charge separation and transfer, and improving overall stability.

3.1.4. HR TEM Analysis. The high-resolution transmission electron microscopy (HR TEM) images provide a detailed morphological and structural assessment of the BiGB5 composite. Figure S2a,b reveals the overall nanostructure, where BiOBr nanosheets are uniformly dispersed over rGO and biochar, indicating successful synthesis. The rGO component is observed as thin, wrinkled, and partially transparent layers intimately interwoven with BiOBr, serving as a conductive framework that enhances electron transport. Biochar appears as a disordered, porous carbonaceous matrix, supporting the anchoring of both BiOBr and rGO and contributing to a high surface area. High-resolution lattice fringe analysis in Figure S2c confirms distinct interplanar spacings of approximately 0.263 and 0.281 nm, corresponding to the (102) and (110) planes of tetragonal BiOBr, respectively. Similarly, the selected area electron diffraction (SAED) pattern of the BiGB5 composite in Figure S2d exhibits distinct diffraction rings, confirming the polycrystalline nature of the composite. The observed rings correspond to the (102), (110), (200), and (212) planes of tetragonal BiOBr, indicating high crystallinity within the composite, which is in accordance with XRD results. The strong interfacial contact among BiOBr, rGO, and biochar observed in the HR TEM images suggests effective nanocomposite formation, which is essential for efficient charge separation and enhanced photocatalytic performance.

3.1.5. XPS Analysis. The chemical composition and elemental oxidation states of the BiGB5 catalyst were investigated using X-ray photoelectron spectroscopy (XPS) analysis and are presented in Fig. 3. The spectral analysis in Figure 3a confirmed the assembly of Bi, Br, O, and C, consistent with the expected composition of the composite. The high-resolution Bi 4f spectrum displayed two prominent peaks at approximately 157.8 and 163.1 eV (Figure 3b), to Bi $4f_{7/7}$ and Bi $4f_{5/2}$, respectively, confirming the presence of Bi^{3+} species within the BiOBr lattice.[30,31] The Br 3d region in Figure 3c exhibited a doublet at around 67.6 and 69.1 eV, which corresponds to Br $3d_{5/2}$ and Br $3d_{3/2}$, confirming the incorporation of bromide ions. The O 1s spectrum featured peaks near 528.6, 530.2, and 532.2 eV, ascribed to lattice

https://doi.org/10.1021/acssusresmgt.5c00430
ACS Sustainable Resour. Manage. XXXX, XXX, XXX−XXX

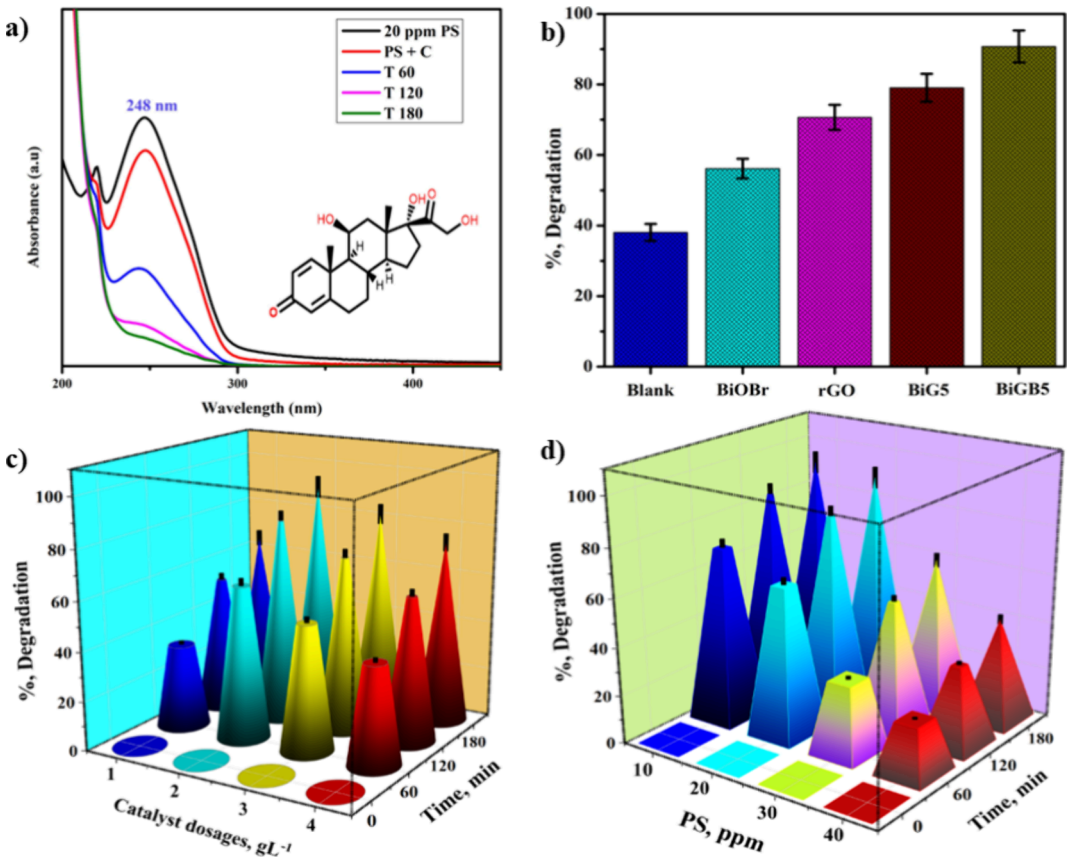

Figure 4. UV−visible spectra of PS in aqueous solution during degradation study (a), the effect of catalyst type (b), BiGB5 concentration (c), and initial PS concentration (d) on the degradation efficiency of PS. Reaction parameters: PS: 20 mg L^{-1}, catalyst: 2 g L^{-1}, duration: 0−180 min.

oxygen and surface oxygen-containing functional groups, respectively (Figure 3d). Additionally, the C 1s spectrum in Figure 3e showed peaks at ∼282.5 eV (sp^2-hybridized C−C/C═C), ∼285.5 eV (C−O) indicative of partially reduced graphene oxide and residual oxygen functionalities from biochar. These results collectively confirm the formation of the BiGB5 composite and the coexistence of BiOBr with conductive carbonaceous materials, which are anticipated to facilitate enhanced charge separation and catalytic performance.

3.1.6. N_2 Adsorption−Desorption Studies. The N_2 adsorption−desorption isotherm of the BiGB5 sample provides insights into its porous structure and surface characteristics, shown in Figure S3a. The surface area and pore volume are found to be 8.9 m^2 g^{-1} and 0.016 ccg^{-1}, respectively. The isotherm displays a Type IV curve with a broad hysteresis loop between $P/P0 \approx 0.1-0.9$, which is indicative of capillary condensation occurring within a wide distribution of meso/macroporous structure. This behavior is typical of nanostructured solids with a highly porous framework or non-uniform structures, where the nanoscale architecture creates abundant surface area and accessible pore channels. In the adsorption branch, the gradual rise in nitrogen uptake at intermediate relative pressures ($P/P0 \approx 0.2-0.8$) reflects multilayer adsorption on the internal surfaces of the nanopores, while the steep rise near $P/P0 \approx 0.9$ suggests capillary condensation within larger mesopores or interparticle voids created by the aggregation of nanoparticles. The accompanying BJH pore size distribution curve lacks long-range ordering, which confirms a wide distribution of mesopore and macropore structure. This nanostructured porosity enhances the surface area of the material, making BiGB5 highly suitable for various applications.

3.1.7. DR UV-Vis and Photoluminescence Studies. The optical absorption properties and bandgap energies of the synthesized catalysts and their composites were systematically studied using DR UV-vis and Tauc plot analyses, as shown in Figure S3a and Figure S3b, respectively. Pristine BiOBr exhibits a distinct absorption edge around 340 nm, corresponding to a wide bandgap of approximately 2.91 eV. In contrast, both rGO and biochar demonstrate strong and broad absorption throughout the UV and visible regions, owing to their extended π-conjugated systems and defect-induced states. Upon compositing BiOBr with rGO and biochar, the resulting BiGB5 and BiG5 hybrids exhibit significantly enhanced absorption in the visible range, indicating strong interfacial electronic interactions that broaden the light absorption profile and promote the utilization of sunlight. The Tauc plots reveal that the BiGB5 composite exhibits a narrowed bandgap of 2.79 eV compared to pristine BiOBr, while rGO and biochar possess very narrow band transitions of 1.25 and 0.87 eV, respectively, reflecting their roles as effective photosensitizers and electron conductors. This bandgap reduction and enhanced light absorption are critical for extending photocatalytic activity into the visible and solar spectrum. The synergistic integration of BiOBr with conductive carbon materials not only improves photon absorption but also facilitates charge separation and transfer, effectively suppressing (e−h) pair recombination.

https://doi.org/10.1021/acssusresmgt.5c00430
ACS Sustainable Resour. Manage. XXXX, XXX, XXX−XXX

Photoluminescence (PL) spectroscopy was employed to investigate the separation efficiency and recombination behaviour of (e−h) pairs in BiOBr, BiG5, and BiGB5 samples, as illustrated in Figure S3d. The PL spectra were recorded at an excitation wavelength of 330 nm, where pristine BiOBr exhibited the highest emission intensity with prominent peaks in the 450−550 nm range. This strong emission is indicative of rapid radiative recombination of charge species, which typically limits its photocatalytic efficiency. In contrast, the PL intensity of the BiG5 composite is significantly reduced, and an even greater quenching effect is observed in the BiGB5 sample. The substantial decrease in PL emission intensity for BiGB5 suggests a more efficient electron-hole separation and migration of charge carriers, which is attributed to the synergistic effect of rGO and biochar within the BiOBr matrix. These carbonaceous components act as electron mediators and conductive pathways, facilitating rapid charge transfer and suppressing recombination.

3.2. Photocatalytic Activity Study of PS. The electronic spectrum of PS in water exhibits an absorption band between 225 and 300 nm, as shown in Figure 4a. This peak primarily results from $n\rightarrow\pi^*$ and $\pi\rightarrow\pi^*$ transitions, which are characteristic of π-conjugated systems and the existence of heteroatoms in the molecule. The characteristic band at λ_{max} of 248 nm was taken as the signature for the identification and determination of PS in the reaction aliquot.[32] When the PS solution was exposed to sunlight for 3 h without any catalyst, about 38% degradation occurred, likely due to photolysis. The photocatalytic efficiency of BiOBr, rGO, BiG5, and BiGB5 was evaluated under sunlight, as shown in Figure 4b. Among them, BiGB5 achieved the highest degradation rate of ∼91%. In comparison, the individual materials showed considerably lower efficiencies, such as BiOBr, rGO, and BiG5, achieving ∼56, ∼70, and ∼79% degradation, respectively. The superior photocatalytic efficiency of BiGB5 was further supported by PL analysis, indicating reduced electron-hole recombination. The time-dependent UV-vis spectra of PS degradation are presented in Figure S7. Total organic carbon (TOC) of PS before the reaction was 30.2 ppm, and after the reaction, it decreased to 6.5 ppm, which also supports the effective degradation of PS (Figure S9, Supporting Information).

3.2.1. Influence of Catalyst Dosage. The impact of varying dosages of BiGB5, ranging from 1 to 4 g L^{-1}, was systematically examined while maintaining a constant PS concentration of 20 mg L^{-1}, as illustrated in Figure 4c. The findings revealed that degradation efficiency initially improved with increasing catalyst dosage from 1 g L^{-1} and achieved an optimal point at 2 g $L^{-1,}$ showing the highest degradation efficiency of ∼91%. However, increasing the catalyst amount, i.e., 3 and 4 g L^{-1}, beyond the optimal dosage did not lead to significant gains rather a decline in degradation efficiency, i.e., ∼82 and ∼74%, respectively. This fall in degradation efficiency after the optimum point is attributed to the aggregation of catalysts at higher dosages, which possibly causes light scattering instead of effective light absorption.

3.2.2. Effect of the PS Concentration. The effect of initial PS concentration on the degradation by BiGB5 is depicted in Figure 4d. As the initial PS concentration increased, the photocatalytic efficiency declined. At lower concentrations of 10 and 20 mg L^{-1}, the degradation efficiency reaches its optimum point, exceeding ∼91% after 3 h. However, at higher concentrations of 30 and 40 mg L^{-1}, the efficiency drops noticeably to ∼61 and ∼42%, respectively. This decrease is ascribed to the saturation of limited active sites and reactive zones on the BiGB5 surface. These observations suggest that the lower concentrations promote easy accessibility to active sites, which induce effective interactions and better adsorption between PS molecules and the catalyst surface, leading to improved degradation efficiencies.

3.2.3. Effect of pH. The effect of pH on the photocatalytic performance of BiGB5 toward PS was evaluated between pH 3 and 9 (Figure S7c, Supporting Information), revealing a clear pH dependence with maximum degradation at pH 6.08. This behaviour correlates with the pH-dependent surface potential of the catalyst. Zeta potential measurements show a progressive increase in negative surface charge from about −10 mV at pH 3 to −21 mV at pH 9, with a moderately negative value (−14.94 mV) at pH 6.08 (Figure S7d, Supporting Information). At this near-neutral pH, the BiGB5 surface is sufficiently negatively charged to promote strong electrostatic attraction and adsorption of positively oriented regions of the pollutant molecules while avoiding excessive repulsion or hindered mass transfer that can occur at extreme pH. Moreover, the moderate magnitude of the negative zeta potential supports good colloidal stability and minimizes particle agglomeration, thereby maximizing accessible active surface area and light penetration. These combined effects, favorable surface charge for pollutant adsorption, effective dispersion of catalyst particles, and enhanced contact between adsorbed substrates and photogenerated charge carriers, which support the superior photocatalytic degradation at pH 6.08.

3.2.4. Heterogeneity and Recyclability. The heterogeneous character of the catalyst was evaluated by performing the degradation reaction using the filtrate obtained after thoroughly washing and removing the catalyst. The observed degradation was approximately 38%, which is consistent with the degradation observed in photolysis experiments. This similarity suggests that the catalytic activity primarily occurs through a heterogeneous mechanism. The reusability of the catalyst was evaluated for five successive cycles, and the results obtained are shown in Figure S8a. In the first cycle (run 1), the catalyst exhibited excellent activity, attaining a mineralization efficiency of ∼91%. Then, subsequently, a gradual decline in activity from 91 to 81% was observed over the next four cycles, indicating minor deactivation likely due to surface fouling or partial loss of active sites. Despite this decline, the catalyst preserved a high activity throughout all five cycles, demonstrating good stability and reusability. These results suggest that the catalyst can be effectively reused multiple times with only a minor decrease in performance, highlighting its potential for practical and cost-effective applications in environmental remediation processes.

3.2.5. Kinetic Study. The catalytic degradation of PS was studied by varying BiGB5 and initial PS concentration to evaluate the kinetic behavior of the reaction. The data obtained showed a strong correlation with the first-order kinetic model, which is given by the following equation:

$$\ln C_t = -kt + \ln C_0 \tag{2}$$

$$\ln\left(\frac{C_t}{C_0}\right) = -kt \tag{3}$$

Here, C_0 represents the initial concentration of PS, C_t denotes the concentration at time t, k is the rate constant, and t is the reaction time measured in min.

https://doi.org/10.1021/acssusresmgt.5c00430
ACS Sustainable Resour. Manage. XXXX, XXX, XXX−XXX

Scheme 2. Plausible Fragmentation Pathway of PS Degradation

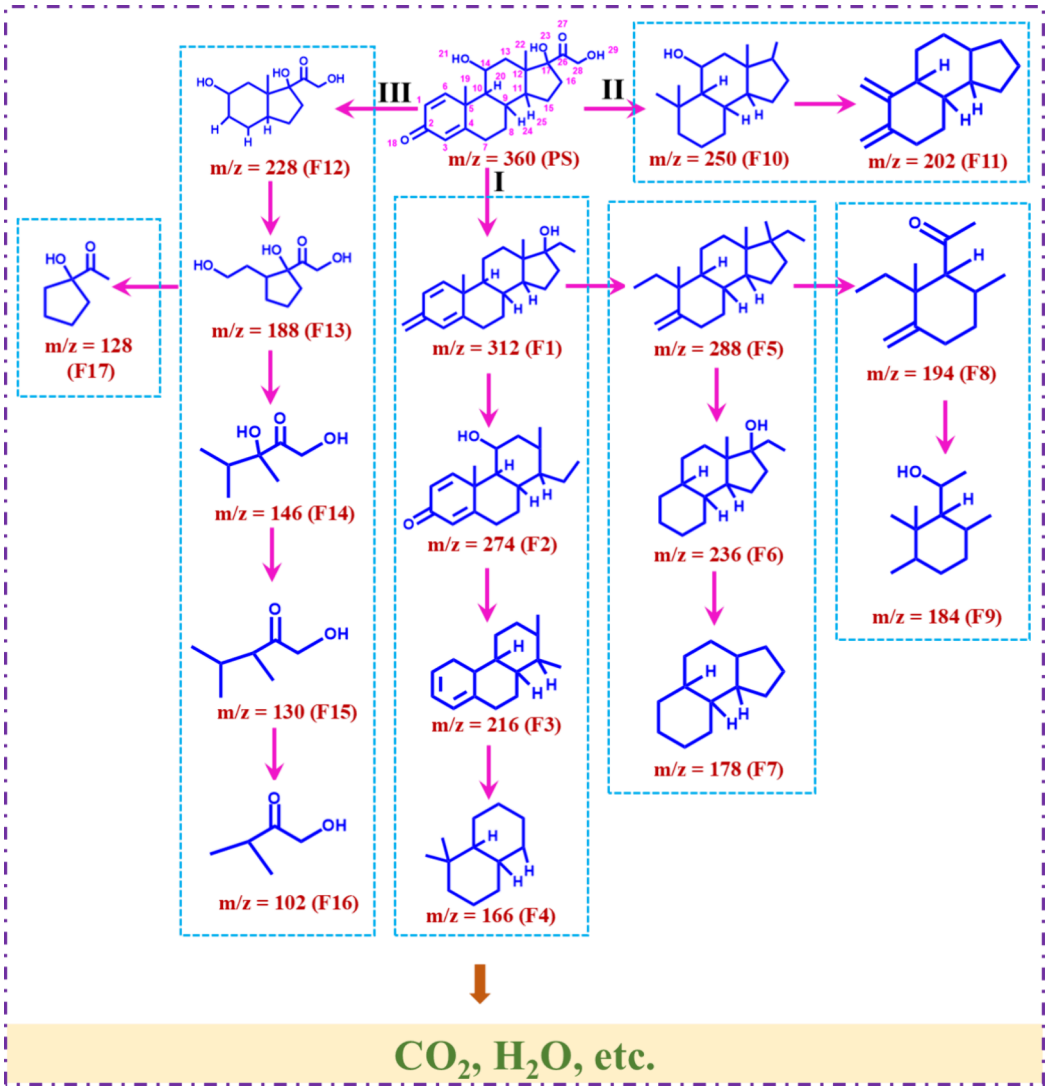

Figure S8b,c illustrates the linear relationship between $\ln(C/C_0)$ and time for various PS and BiGB5 concentrations, confirming first-order reaction kinetics.[33,34] The strong correlation ($R^2 \geq 0.98$) for all conditions supports this conclusion (Table S6). The slope of each line represents the apparent first-order rate constant (k), which showed a slight decrease as the initial PS concentration increased. This trend suggests a possible reduction in catalytic efficiency at higher concentrations, likely due to competitive adsorption of PS molecules on the BiGB5 surface. Similarly, with a rise in BiGB5 dosages, the rate constant increased until a certain point and then decreased due to possible aggregation of BiGB5 particles, leading to light scattering.

3.2.6. Scavenger Study. Various scavengers were used to detect the specific reactive species participating in the photocatalytic degradation method. Potassium iodide (KI) and isopropyl alcohol (IPA) were used as the scavengers for hydroxyl radicals, whereas benzoquinone (BQ) and sodium oxalate ($Na_2C_2O_4$) were used as specific scavengers for superoxide radicals and photogenerated holes, respectively.[35,36] In the absence of any scavenger, the degradation percentage was ~91%, indicating excellent photocatalytic activity. All scavengers were used at a concentration of 5 mM, and the obtained outcomes are presented in Figure S8d. When KI was added, the degradation significantly dropped to approximately 46%, indicating the crucial role of surface hydroxyl radicals in the process. Similarly, the use of IPA led to a decrease in degradation, ~67%, corresponding to the scavenging of hydroxyl radicals in the reaction medium. The addition of BQ, a superoxide radical scavenger, led to a minimal decrease of ~76%, suggesting the involvement of superoxide radicals to a lesser extent. Sodium oxalate showed a minor reduction in activity, ~77%, indicating the less dominant participation of photogenerated holes. These results collectively highlight hydroxyl radicals as the major radical species in the mineralization process.

3.2.7. Intermediates and Plausible Degradation Pathway of PS. The degradation intermediates of PS were analyzed through liquid chromatography mass spectrometry (LCMS), and the corresponding mass spectral data are provided in Figures S10 and S11. Specific functional groups within the PS structure, particularly hydroxyl groups, conjugated double bonds, and carbonyl moieties, exhibit high electron density and are therefore prone to oxidative attack by reactive species generated under photocatalytic conditions.[37,38] Based on the detected intermediates, a three-pathway degradation mecha-

https://doi.org/10.1021/acssusresmgt.5c00430
ACS Sustainable Resour. Manage. XXXX, XXX, XXX−XXX

nism was proposed, as depicted in Scheme 2. These routes involve a sequence of oxidative transformations, including hydroxylation, ring cleavage, and side-chain scission, progressively breaking down the parent molecule into smaller intermediates and eventually mineralizing, possibly into carbon dioxide, water, and short-chain organic compounds. The photocatalytic degradation of PS proceeds through a complex sequence of oxidative transformations, yielding 17 identifiable intermediate fragments. In path I, initially, the hydroxyl radicals generated under photocatalytic conditions attack the steroid nucleus, leading to hydroxylation at key reactive sites such as C11, C14, and C21, forming mono- and dehydroxylated intermediates like F1 (m/z = 312) and F2 (m/z = 274). These hydroxyl groups are subsequently oxidized to ketone functionalities, increasing the electrophilicity of the adjacent carbon atoms and facilitating ring-opening and ring-cleavage reactions to form fragments F3 (m/z = 216) and F4 (m/z = 166). Simultaneously, the C2 and C3 sites undergo oxidation and cleavage to form the intermediate F5 (m/z = 288), which further undergoes dehydroxylation and radical attack, leading to smaller fragments such as F6 (m/z = 236) and F7 (m/z = 178). The oxidative cleavage of F5 leads to the formation of a carboxylic acid (F8), followed by smaller steroidal fragments (F9). Similarly, in path II, the carbonyl carbon at C2 undergoes decarbonylation along with ring opening with a series of reactions to yield the fragments F10 (m/z = 250) and F11 (m/z = 202). Path III involves the formation of intermediate products such as short-chain carboxylic acids and open-ring steroid derivatives from F12 (m/z = 228). Continued oxidative fragmentation breaks down the steroid skeleton into smaller molecules like diacids, aldehydes, and unsaturated carbonyl compounds (F11−F17). In the final stages, these low molecular weight intermediates undergo complete mineralization through successive decarboxylation, dehydrogenation, and hydration reactions, ultimately forming stable end products such as carbon dioxide, water, and simple organic compounds.

3.2.8. Proposed Charge Transfer Mechanism. The proposed photocatalytic degradation mechanism of PS using the BiGB5 ternary nanocomposite under sunlight is illustrated in Scheme 3. Upon exposure to sunlight, BiOBr is photoexcited to generate (e^-−h^+) pairs. The CB potential of the BiOBr is 0.3 eV vs. NHE, while the VB potential is around +3.1 eV vs. NHE. Since the reduction potential of $O_2/\bullet O_2^-$ is −0.33 eV and the oxidation potential of $OH^-/\bullet OH$ is +2.8 eV (both vs. NHE at pH 7), the VB of BiOBr is more positive than +2.8 eV.[39] This indicates that the photogenerated holes have sufficient thermodynamic potential to generate •OH radicals. On the other hand, the $\bullet O_2^-$ radicals produced may be attributed to the integration of rGO in the composite.[40]

$$\text{BiOBr/rGO/Biochar} + h\nu \rightarrow \text{BiOBr/rGO/Biochar}(h^+_{VB} + e^-_{CB}) \quad (4)$$

$$\text{BiOBr}(h^+_{VB}) + H_2O \rightarrow \bullet OH + H^+ \quad (5)$$

$$\text{rGO}(e^-_{CB}) + O_2 \rightarrow \bullet O_2^- \quad (6)$$

$$\text{BiOBr, rGO}(e^-_{CB}) + \bullet O_2^- + 2H^+ \rightarrow H_2O_2 \quad (7)$$

$$\text{BiOBr, rGO}(e^-_{CB}) + H_2O_2 + H^+ \rightarrow \bullet OH + H_2O \quad (8)$$

Scheme 3. Proposed Charge Transfer Mechanism in BiGB5 during Photocatalytic Reaction

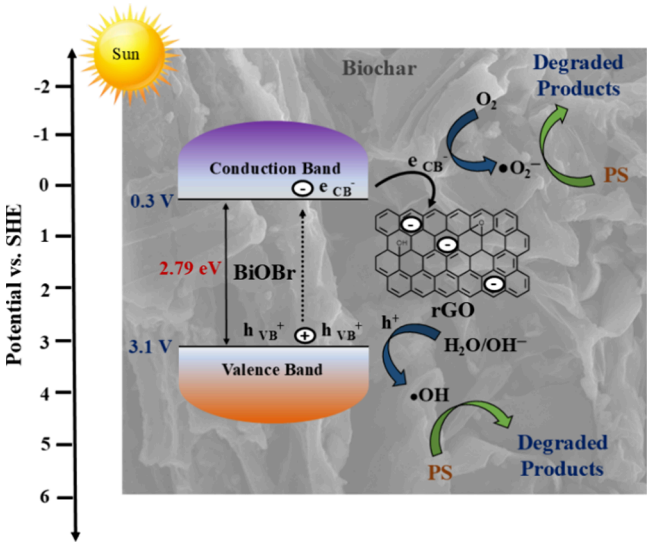

$$\text{Prednisolone} + \bullet OH + \bullet O_2^- \rightarrow CO_2 + H_2O + \text{Smallmolecule} \quad (9)$$

Photoexcited electrons from the CB of BiOBr migrate to rGO, which acts as an electron mediator in the photocatalytic system due to its π-conjugated carbon domains and helps in reducing the electron-hole recombination.[41,16] Biochar functions both as a conductive and porous carbon framework that provides abundant active sites and improves charge separation. This reduced recombination enables the preservation of highly oxidative h^+ in the VB of BiOBr, which oxidizes water or hydroxide ions to produce •OH radical. The electrons in rGO/biochar are efficiently transferred to surface-adsorbed oxygen molecules, forming reactive superoxide radicals ($\bullet O_2^-$). These species play a crucial role in the oxidative cleavage of PS, initiating hydroxylation, oxidative ring cleavage, and progressive breakdown into smaller, less toxic intermediates, eventually mineralizing to CO_2 and H_2O. The synergistic integration of BiOBr, rGO, and biochar not only improves charge carrier dynamics but also enhances light absorption and active site availability, leading to superior photocatalytic performance.

4. CONCLUSIONS

This work demonstrates a simple and sustainable approach for designing a highly efficient ternary nanocomposite biochar-integrated BiOBr/rGO for the efficient oxidative degradation of the persistent pharmaceutical contaminant prednisolone under sunlight. The synthesized nanocomposite leverages the synergistic properties of each component, where BiOBr provides visible-light photoactivity, rGO enhances charge transport and electron mobility, and biochar, derived from biomass waste, serves as a porous, conductive, and environmentally benign support that promotes electron transfer and adsorption of organic pollutants. The incorporation of biochar not only increased the specific surface area and active site availability but also embodied a waste-to-resource strategy by converting biomass residues into functional photocatalytic materials. Mechanistic investigations, supported by radical scavenging experiments, identified hydroxyl radicals (•OH) as

https://doi.org/10.1021/acssusresmgt.5c00430
ACS Sustainable Resour. Manage. XXXX, XXX, XXX−XXX

the primary reactive species driving the oxidative degradation process. LC MS analyses revealed intermediate degradation products, allowing the proposal of a plausible degradation pathway for prednisolone. The nanocomposite exhibited excellent reusability, stability, and potential for complete mineralization of toxic intermediates under solar irradiation. Overall, this study demonstrated the promise of biochar-based ternary photocatalysts as low-cost, sustainable, and highly effective materials for the mineralization of emerging pollutants. It also reinforces the value of circular economy strategies in transforming biomass waste into high-value functional materials for clean water technologies.

■ ASSOCIATED CONTENT

Data Availability Statement

Data underlying the results of this study can be obtained from the corresponding author upon reasonable request.

Supporting Information

The Supporting Information is available free of charge at https://pubs.acs.org/doi/10.1021/acssusresmgt.5c00430.

Experimental: reagents and chemicals, preparation of reduced graphene oxide, preparation of biochar from banana peels, characterization, and photocatalytic degradation studies of PS; result and discussion: HR TEM images, N_2 adsorption-desorption isotherm, UV-vis DRS spectra, Tauc plot, and PL spectra, TGA and DTA, optimized structures of PS, time-dependent UV-vis spectra of PS degradation and its kinetic plot, effect of pH on catalytic efficiency, and zeta potential of BiGB5 at different pH, relationship table between rate constant with BiGB5 and PS dosages, recycling of catalyst, kinetic study, effect of scavengers, TOC data of PS before and after reaction, and mass spectrogram of PS degradation (PDF)

■ AUTHOR INFORMATION

Corresponding Author

Sushanta Kumar Badamali − *Department of Chemistry, Utkal University, Bhubaneswar, Odisha 751004, India;* orcid.org/0000-0003-0526-0146; Email: skbuche@utkaluniversity.ac.in

Authors

Mano Ranjan Barik − *Department of Chemistry, Utkal University, Bhubaneswar, Odisha 751004, India*

Ankita Ram − *Department of Chemistry, Utkal University, Bhubaneswar, Odisha 751004, India*

Complete contact information is available at: https://pubs.acs.org/10.1021/acssusresmgt.5c00430

Author Contributions

Mano Ranjan Barik: investigation, methodology, material preparation, software, writing—original draft, and data curation. Ankita Ram: material preparation and investigation. Sushanta Kumar Badamali: supervision, conceptualization, resources, methodology, formal analysis, and writing—review and editing.

Notes

The authors declare no competing financial interest.

■ ACKNOWLEDGMENTS

M.R.B. expresses sincere gratitude to the Centre of Advanced Materials and Applications, Department of Chemistry, Utkal University, for providing research facilities. M.R.B. gratefully acknowledges the extended support of the Central Research Facility, KIIT University, for conducting XRD, FE SEM, and LC MS analyses, and to IIT Hyderabad for assistance with XPS analysis. M.R.B. is also grateful to CSIR-IMMT for the TOC measurement. M.R.B. is thankful to the University Grants Commission, Government of India, for granting Senior Research Fellowship.

■ REFERENCES

(1) Kwa, M.; Guttentag, A.; Chase, L.; van Meijgaard, J.; Lim, H. W. Trends in Price for Topical Corticosteroids from 2017 to 2021 and the Opportunity for Cost Savings Identifiable at the Point of Care: A Retrospective Cross-Sectional Study. *J. Am. Acad. Dermatol.* **2024**, *90* (1), 74−81.

(2) Cox, L.; Gibbs, N.; Turnock, L. A. Emerging Anabolic Androgenic Steroid Markets: The Prominence of Social Media. *Drugs Educ. Prev. Policy* **2024**, *31* (2), 257−270.

(3) Krasselt, M.; Baerwald, C. The Current Relevance and Use of Prednisone in Rheumatoid Arthritis. *Expert Rev. Clin. Immunol.* **2014**, *10* (5), 557−571.

(4) Ichai, P.; Duclos-Vallée, J. C.; Guettier, C.; Hamida, S. B.; Antonini, T.; Delvart, V.; Saliba, F.; Azoulay, D.; Castaing, D.; Samuel, D. Usefulness of Corticosteroids for the Treatment of Severe and Fulminant Forms of Autoimmune Hepatitis. *Liver Transplant.* **2007**, *13* (7), 996−1003.

(5) Weizel, A.; Schlüsener, M. P.; Dierkes, G.; Ternes, T. A. Occurrence of Glucocorticoids, Mineralocorticoids, and Progestogens in Various Treated Wastewater, Rivers, and Streams. *Environ. Sci. Technol.* **2018**, *52* (9), 5296−5307.

(6) Richards, R. N. Side Effects of Short-Term Oral Corticosteroids. *J. Cutan. Med. Surg.* **2008**, *12* (2), 77−81.

(7) Bollet, A. J.; Black, R.; Bunim, J. J. Major Undesirable Side-Effects Resulting from Prednisolone and Prednisone. *JAMA* **1955**, *158* (6), 459−463.

(8) Allen, D. B.; Bielory, L.; Derendorf, H.; Dluhy, R.; Colice, G. L.; Szefler, S. J. Inhaled Corticosteroids: Past Lessons and Future Issues. *J. Allergy Clin. Immunol.* **2003**, *112* (3), S1−S40.

(9) Hanafi, M. F.; Sapawe, N. A Review on the Current Techniques and Technologies of Organic Pollutants Removal from Water/Wastewater. *Mater. Today Proc.* **2020**, *31*, A158−A165.

(10) Mahlambi, M. M.; Ngila, C. J.; Mamba, B. B. Recent Developments in Environmental Photocatalytic Degradation of Organic Pollutants: The Case of Titanium Dioxide Nanoparticles A Review. *J. Nanomater.* **2015**, *2015* (1), No. 790173.

(11) Klauson, D.; Pilnik-Sudareva, J.; Pronina, N.; Budarnaja, O.; Krichevskaya, M.; Käkinen, A.; Juganson, K.; Preis, S. Aqueous Photocatalytic Oxidation of Prednisolone. *Open Chem.* **2013**, *11* (10), 1620−1633.

(12) Wang, L.; Yu, J. Principles of Photocatalysis. In *Interface Science and Technology*; Elsevier, 2023; *35* pp 1−52.

(13) Saravanan, R.; Gracia, F.; Stephen, A. Basic Principles, Mechanism, and Challenges of Photocatalysis. In *Nanocomposites for Visible Light-Induced Photocatalysis*; Springer International Publishing: Cham, 2017; pp 19−40.

(14) Barik, M. R.; Kumar, J.; Badamali, S. K. *Nyctanthes arbor-tristis* L. Mediated Sustainable Synthesis of α-Fe_2O_3/g-C_3N_4 S-Scheme Heterojunctions for Enhanced Photocatalytic Degradation of Tetracycline Hydrochloride: A Mechanistic Insight and DFT Study. *RSC Sustainable* **2025**, 3582.

(15) Feng, H.; Xu, Z.; Wang, L.; Yu, Y.; Mitchell, D.; Cui, D.; Xu, X.; Shi, J.; Sannomiya, T.; Du, Y.; Hao, W.; Dou, S. X. Modulation of Photocatalytic Properties by Strain in 2D BiOBr Nanosheets. *ACS Appl. Mater. Interfaces* **2015**, *7* (50), 27592−27596.

(16) Mohd Kaus, N. H.; Rithwan, A. F.; Adnan, R.; Ibrahim, M. L.; Thongmee, S.; Mohd Yusoff, S. F. Effective Strategies, Mechanisms, and Photocatalytic Efficiency of Semiconductor Nanomaterials Incorporating rGO for Environmental Contaminant Degradation. *Catalysts* **2021**, *11* (3), 302.
(17) Mian, M. M.; Liu, G. Recent Progress in Biochar-Supported Photocatalysts: Synthesis, Role of Biochar, and Applications. *RSC Adv.* **2018**, *8* (26), 14237−14248.
(18) Cacciari, R. D.; Reynoso, E.; Montejano, H. A.; Biasutti, M. A. Photodegradation of Prednisolone under UVB Solar Irradiation: Role of Photogenerated ROS in the Degradation Mechanism. *Photochem. Photobiol. Sci.* **2017**, *16*, 1717−1726.
(19) Yin, K.; He, Q.; Liu, C.; Deng, Y.; Wei, Y.; Chen, S.; Liu, T.; Luo, S. Prednisolone Degradation by UV/Chlorine Process: Influence Factors, Transformation Products and Mechanism. *Chemosphere* **2018**, *212*, 56−66.
(20) Mohammadi, S.; Zarei, M.; Amini-Fazl, M. S.; Ebratkhahan, M. Removal and Mineralization of Prednisolone from Water by Using Homogeneous and Heterogeneous Electro-Fenton Processes. *J. Environ. Chem. Eng.* **2023**, *11* (5), No. 110465.
(21) Mei, X.; Meng, X.; Wu, F. Hydrothermal Method for the Production of Reduced Graphene Oxide. *Phys. E Low-Dimens. Syst. Nanostruct.* **2015**, *68*, 81−86.
(22) Nadew, T. T.; Keana, M.; Sisay, T.; Getye, B.; Habtu, N. G. Synthesis of Activated Carbon from Banana Peels for Dye Removal of an Aqueous Solution in Textile Industries: Optimization, Kinetics, and Isotherm Aspects. *Water Pract. Technol.* **2023**, *18* (4), 947−966.
(23) Cao, F.; Wang, J.; Wang, Y.; Zhou, J.; Li, S.; Qin, G.; Fan, W. An *In Situ* Bi-Decorated BiOBr Photocatalyst for Synchronously Treating Multiple Antibiotics in Water. *Nanoscale Adv.* **2019**, *1* (3), 1124−1129.
(24) Wang, Y.; Shi, Z.; Fan, C.; Wang, X.; Hao, X.; Chi, Y. Synthesis, Characterization, and Photocatalytic Properties of BiOBr Catalyst. *J. Solid State Chem.* **2013**, *199*, 224−229.
(25) Zhang, P.; O'Connor, D.; Wang, Y.; Jiang, L.; Xia, T.; Wang, L.; Tsang, D. C. W.; Ok, Y. S.; Hou, D. A Green Biochar/Iron Oxide Composite for Methylene Blue Removal. *J. Hazard. Mater.* **2020**, *384*, No. 121286.
(26) Habte, A. T.; Ayele, D. W. Synthesis and Characterization of Reduced Graphene Oxide (rGO) Started from Graphene Oxide (GO) Using the Tour Method with Different Parameters. *Adv. Mater. Sci. Eng.* **2019**, *2019* (1), 1.
(27) Priyanka; Vashisht, D.; Ibhadon, A. O.; Mehta, S. K.; Taylor, M. J. Enhanced Wastewater Remediation Using Mesoporous Activated Wheat Straw Biochars: A Dye Removal Perspective. *ACS Sustainable Resource Management* **2024**, *1* (2), 355−367.
(28) Tu, X.; Luo, S.; Chen, G.; Li, J. One-Pot Synthesis, Characterization, and Enhanced Photocatalytic Activity of a BiOBr−Graphene Composite. *Chem. - Eur. J.* **2012**, *18* (45), 14359−14366.
(29) Sharma, N.; Sharma, V.; Jain, Y.; Kumari, M.; Gupta, R.; Sharma, S. K.; Sachdev, K. Synthesis and Characterization of Graphene Oxide (GO) and Reduced Graphene Oxide (rGO) for Gas Sensing Application. *Macromol. Symp.* **2017**, *376* (1), 1700006.
(30) Shkir, M.; Aldirham, S. H.; AlFaify, S.; Ali, A. M. A Novel BiOBr/rGO Photocatalysts for Degradation of Organic and Antibiotic Pollutants under Visible Light Irradiation: Tetracycline Degradation Pathways, Kinetics, and Mechanism Insight. *Chemosphere* **2024**, *357*, No. 141934.
(31) Gao, Z.; Yao, B.; Yang, F.; Xu, T.; He, Y. Preparation of BiOBr−Bi Heterojunction Composites with Enhanced Photocatalytic Properties on BiOBr Surface by In-Situ Reduction. *Mater. Sci. Semicond. Process.* **2020**, *108*, No. 104882.
(32) Bhusnure, O. G.; Bawage, M. S.; Gholve, S. B. Eco-Friendly and Cost-Effective UV Spectroscopy Method for the Estimation of Prednisolone Sodium Phosphate in Bulk and Pharmaceutical Dosage Form. *Int. J. Pharm. Sci. Res.* **2015**, *6* (1), 327.
(33) Barik, M. R.; Badamali, S. K. A Comparative Study on the Sunlight-Assisted Photocatalytic Efficiency of TiO_2 in the Mineralization of Ofloxacin: Kinetics and Degradation Pathways. *ChemistrySelect* **2025**, *10* (25), No. e01792.
(34) Bhoi, B.; Chandra, V. Highly Efficient Degradation of Toxic Congo Red Dye under Sunshine Using a Mesoporous $BiZnO_3$/g-C_3N_4 Nanocomposite. *ACS Sustainable Resource Management* **2025**, *2* (5), 744−754.
(35) Jangir, L. K.; Tripathi, V. K.; Kumari, P.; Shrivastava, M.; Sharma, Y. C.; Tripathi, K. M. MoS_2 Decorated 3D Graphene Aerogel as a Microwave Catalyst for the Ultrafast Breakdown of Organic Dyes. *ACS Sustainable Resource Management* **2025**, *2* (6), 1130−1138.
(36) Rodriguez, E. M.; Marquez, G.; Tena, M.; Álvarez, P. M.; Beltran, F. J. Determination of Main Species Involved in the First Steps of TiO_2 Photocatalytic Degradation of Organics with the Use of Scavengers: The Case of Ofloxacin. *Appl. Catal., B* **2015**, *178*, 44−53.
(37) Xiong, L.; Tang, J. Strategies and Challenges on Selectivity of Photocatalytic Oxidation of Organic Substances. *Adv. Energy Mater.* **2021**, *11* (8), 2003216.
(38) Molla, M. A. I.; Ahmed, A. Z.; Kaneco, S. Reaction Mechanism for Photocatalytic Degradation of Organic Pollutants. In *Nanostructured Photocatalysts*; Elsevier, 2021; pp 63−84.
(39) Xu, Q.; Zhang, L.; Cheng, B.; Fan, J.; Yu, J. S-Scheme Heterojunction Photocatalyst. *Chem.* **2020**, *6* (7), 1543−1559.
(40) Mondal, A.; Prabhakaran, A.; Gupta, S.; Subramanian, V. R. Boosting Photocatalytic Activity Using Reduced Graphene Oxide (RGO)/Semiconductor Nanocomposites: Issues and Future Scope. *ACS Omega* **2021**, *6* (13), 8734−8743.
(41) Jo, W. K.; Selvam, N. C. S. Z-Scheme CdS/g-C_3N_4 Composites with RGO as an Electron Mediator for Efficient Photocatalytic H_2 Production and Pollutant Degradation. *Chem. Eng. J.* **2017**, *317*, 913−924.

https://doi.org/10.1021/acssusresmgt.5c00430
ACS Sustainable Resour. Manage. XXXX, XXX, XXX−XXX